

# Supporting Information for “Seismic shear waves as Foucault pendulum” (2015GL067598)

Roel Snieder<sup>1,2</sup>, Christoph Sens-Schönfelder<sup>2</sup>, Elmer Ruigrok<sup>3,4</sup>,  
and Katsuhiko Shiomi<sup>5</sup>

(1) Center for Wave Phenomena, Colorado School of Mines, Golden, USA

(2) GFZ German Research Centre for Geosciences, Potsdam, Germany

(3) Dept. of Earth Sciences, Utrecht University, Utrecht, Netherlands

(4) R&D Seismology and Acoustics, Royal Netherlands Meteorological Institute (KNMI), De Bilt, Netherlands

(5) NIED National Research Institute for Earth Science and Disaster Prevention, Tsukuba, Japan

Section 1 gives the derivation of the polarization of body waves in a rotating medium as inferred from the Christoffel equation. An estimate of the order of magnitude the ray bending for *ScS2* waves propagating through a horizontal velocity gradient in the upper mantle is given in section 2. We show in section 3 the data and the used processing.

## 1 PLANE ELASTIC WAVES IN A ROTATING SYSTEM

We consider the special case of a homogeneous isotropic elastic medium and assume that the rotation rate is small, in the sense that  $\Omega/\omega \ll 1$ , where  $\omega$  is the angular frequency of the waves. All results are accurate to first order in  $\Omega/\omega$ . The equation of motion in an homogeneous elastic medium follows from expression (4.1) of *Aki and Richards (2002)*

$$\rho \ddot{\mathbf{u}} = (\lambda + \mu) \nabla (\nabla \cdot \mathbf{u}) + \mu \nabla^2 \mathbf{u} - 2\rho \boldsymbol{\Omega} \times \dot{\mathbf{u}}, \quad (1)$$

where  $\rho$  is the mass density,  $\lambda$  and  $\mu$  the Lamé parameters, and the overdot denotes a time-derivative. We added the last term, which accounts for the Coriolis force. Note that we have not included the centrifugal force  $-\rho \boldsymbol{\Omega} \times (\boldsymbol{\Omega} \times \mathbf{r})$  because this force gives a contribution  $O(\Omega/\omega)^2$ , which we ignore. We seek solutions of the form

$$\mathbf{u} = \hat{\mathbf{q}} e^{i(k\hat{\mathbf{n}} \cdot \mathbf{r} - \omega t)}, \quad (2)$$

where the unit vector  $\hat{\mathbf{n}}$  gives the direction of propagation and  $\hat{\mathbf{q}}$  the polarization. Inserting this in expression (1) gives the Christoffel equation in a rotating system

$$\hat{\mathbf{q}} = \frac{\lambda + \mu}{\rho c^2} \hat{\mathbf{n}} (\hat{\mathbf{n}} \cdot \hat{\mathbf{q}}) + \frac{\mu}{\rho c^2} \hat{\mathbf{q}} - \frac{2i}{\omega} \boldsymbol{\Omega} \times \hat{\mathbf{q}}, \quad (3)$$

where  $c = \omega/k$  is the wave velocity.

We define a coordinate system to describe the polarization as shown in figure 1. We choose the  $z$ -axis in the direction of wave propagation ( $\hat{\mathbf{z}} = \hat{\mathbf{n}}$ ), and define

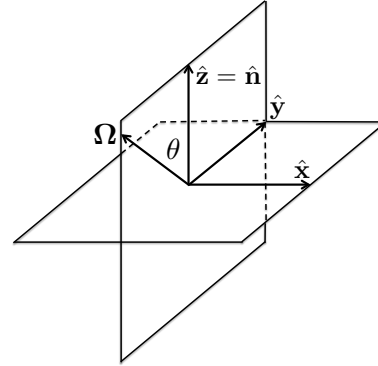


**Figure 1.** Definition of the unit vectors  $\hat{\mathbf{x}}$ ,  $\hat{\mathbf{y}}$ ,  $\hat{\mathbf{z}}$  and the angle  $\theta$ .

the unit vector  $\hat{\mathbf{x}}$  in the direction of  $\hat{\mathbf{z}} \times \boldsymbol{\Omega}$ . The last unit vector is defined by  $\hat{\mathbf{y}} = \hat{\mathbf{z}} \times \hat{\mathbf{x}}$ , so that the system  $\hat{\mathbf{x}}$ ,  $\hat{\mathbf{y}}$ ,  $\hat{\mathbf{z}}$  is right-handed. The angle between the rotation vector and the direction of wave propagation is denoted by  $\theta$ . The vectors  $\hat{\mathbf{x}}$  and  $\hat{\mathbf{y}}$  are given by

$$\hat{\mathbf{x}} = (\hat{\mathbf{z}} \times \hat{\boldsymbol{\Omega}}) / \sin \theta \quad \text{and} \quad \hat{\mathbf{y}} = (\cos \theta \hat{\mathbf{z}} - \hat{\boldsymbol{\Omega}}) / \sin \theta. \quad (4)$$

We write the polarization vector as a superposition of the basis vectors:

$$\hat{\mathbf{q}} = q_x \hat{\mathbf{x}} + q_y \hat{\mathbf{y}} + q_z \hat{\mathbf{z}}. \quad (5)$$

When using this expansion in the Christoffel equation (3) one needs the cross product of the rotation vector with the basis vectors. It follows from expression (4) that

$$\begin{aligned} \boldsymbol{\Omega} \times \hat{\mathbf{x}} &= \Omega \sin \theta \hat{\mathbf{z}} + \Omega \cos \theta \hat{\mathbf{y}}, \\ \boldsymbol{\Omega} \times \hat{\mathbf{y}} &= -\Omega \cos \theta \hat{\mathbf{x}}, \\ \boldsymbol{\Omega} \times \hat{\mathbf{z}} &= -\Omega \sin \theta \hat{\mathbf{x}}. \end{aligned} \quad (6)$$

Inserting the expansion (5) into the Christoffel equation (3), using expressions (6), and collecting the coefficients multiplying  $\hat{\mathbf{x}}$ ,  $\hat{\mathbf{y}}$ , and  $\hat{\mathbf{z}}$  gives

$$\begin{aligned} \left(\frac{\mu}{\rho c^2} - 1\right) q_x + \frac{2i\Omega}{\omega} (\sin\theta q_z + \cos\theta q_y) &= 0, \\ \left(\frac{\mu}{\rho c^2} - 1\right) q_y - \frac{2i\Omega}{\omega} \cos\theta q_x &= 0, \\ \left(\frac{\lambda + 2\mu}{\rho c^2} - 1\right) q_z - \frac{2i\Omega}{\omega} \sin\theta q_x &= 0. \end{aligned} \quad (7)$$

### 1.1 The polarization of $P$ -waves

Since the imprint of the rotation is assumed to be small ( $\Omega/\omega \ll 1$ ) the  $P$ -waves have a polarization that is close to longitudinal. This means that  $q_z = 1$  and that  $q_x$  and  $q_y$  are small. Since the polarization vector is a unit vector, it is to first order only perturbed in the transverse direction, therefore  $q_z$  is not perturbed. The velocity is close to the  $P$ -wave velocity in an unrotating medium, hence

$$c_P = \sqrt{\frac{\lambda + 2\mu}{\rho}} + \delta c_P, \quad (8)$$

with  $\delta c_P \ll c_P$ . Using a first order Taylor expansion

$$\frac{1}{c_P^2} = \frac{\rho}{\lambda + 2\mu} \left(1 - 2\frac{\delta c_P}{c_P}\right), \quad (9)$$

Inserting this in expression (7) gives

$$\begin{aligned} \frac{\lambda + \mu}{\lambda + 2\mu} q_x - \frac{2i\Omega}{\omega} \cos\theta q_y &= \frac{2i\Omega}{\omega} \sin\theta, \\ \frac{2i\Omega}{\omega} \cos\theta q_x + \frac{\lambda + \mu}{\lambda + 2\mu} q_y &= 0, \\ \frac{2i\Omega}{\omega} \sin\theta q_x &= -2\frac{\delta c_P}{c_P}. \end{aligned} \quad (10)$$

Since  $q_x$  and  $q_y$  are small, we ignore the products  $(\Omega/\omega)q_x$  and  $(\Omega/\omega)q_y$  in the first two lines, which gives

$$q_x = \frac{2i\Omega}{\omega} \frac{\lambda + 2\mu}{\lambda + \mu} \sin\theta, \quad q_y = 0. \quad (11)$$

With  $q_z = 1$  this gives the polarization vector for the  $P$ -waves:

$$\hat{\mathbf{q}}_P = \hat{\mathbf{z}} + \frac{2i\Omega \sin\theta}{\omega} \frac{\lambda + 2\mu}{\lambda + \mu} \hat{\mathbf{x}}. \quad (12)$$

Using the geometry of figure 1 this can also be written as

$$\hat{\mathbf{q}}_P = \hat{\mathbf{z}} + \frac{2i}{\omega} \frac{\lambda + 2\mu}{\lambda + \mu} \hat{\mathbf{z}} \times \boldsymbol{\Omega}. \quad (13)$$

The velocity follows by inserting  $q_x$  from expression (11) into the first line of equation (10)

$$\frac{\delta c_P}{c_P} = 2 \frac{\lambda + 2\mu}{\lambda + \mu} \left(\frac{\Omega \sin\theta}{\omega}\right)^2, \quad (14)$$

which means that

$$c_P = \sqrt{\frac{\lambda + 2\mu}{\rho}} + O(\Omega/\omega)^2. \quad (15)$$

The last expression simply states that the wave velocity of  $P$ -waves is to first order in  $\Omega/\omega$  not affected by Earth's rotation. According to equation (12) the polarization is not purely in the direction of propagation; the  $P$ -wave has a small transverse component. In acoustic media the polarization of  $P$ -waves is also affected by Earth's rotation and setting  $\mu = 0$  in expression (13) gives a  $P$ -wave polarization  $\hat{\mathbf{q}}_P = \hat{\mathbf{z}} + (2i/\omega) \hat{\mathbf{z}} \times \boldsymbol{\Omega}$ .

### 1.2 The circular polarization of $S$ -waves

For the  $S$ -waves the longitudinal polarization is small, so we use that  $q_z$  is small. The shear velocity is given by

$$c_S = \sqrt{\frac{\mu}{\rho}} + \delta c_S. \quad (16)$$

Using a first order Taylor expansion in the perturbation  $\delta c_S$

$$\frac{1}{c_S^2} = \frac{\rho}{\mu} \left(1 - 2\frac{\delta c_S}{c_S}\right). \quad (17)$$

Inserting this in expression (7) and, ignoring cross terms  $(\delta c_S/c_S)q_z$  and  $(\Omega/\omega)q_z$ , gives

$$\begin{aligned} \frac{\delta c_S}{c_S} q_x &= +\frac{i\Omega}{\omega} \cos\theta q_y, \\ \frac{\delta c_S}{c_S} q_y &= -\frac{i\Omega}{\omega} \cos\theta q_x, \\ \frac{\lambda + \mu}{\mu} q_z &= \frac{2i\Omega}{\omega} \sin\theta q_x. \end{aligned} \quad (18)$$

Inserting the equation of the middle line into the first expression gives  $(\delta c_S/c_S)^2 = ((\Omega/\omega) \cos\theta)^2$ , or

$$\frac{\delta c_S}{c_S} = \pm \frac{\Omega}{\omega} \cos\theta. \quad (19)$$

For the + sign, equation (18) predicts that  $q_y = -iq_x$ , so the normalized polarization vector in the transverse plane is given by  $\hat{\mathbf{q}}_S = \hat{\mathbf{x}} - i\hat{\mathbf{y}}$ . For the - sign in expression (19), equation (18) states that  $q_y = +iq_x$ , hence the polarization in the transverse plane is given by  $\hat{\mathbf{q}}_S = \hat{\mathbf{x}} + i\hat{\mathbf{y}}$ .

Both transverse polarizations are circular. The first line of expression (18) states the the  $S$ -waves have a small longitudinal component that is for the used value  $q_x = 1$  given by the last line of expression (18)

$$q_z = \frac{2i\Omega \sin\theta}{\omega} \frac{\mu}{\lambda + \mu}. \quad (20)$$

For the  $S$ -waves there are thus two solutions that are

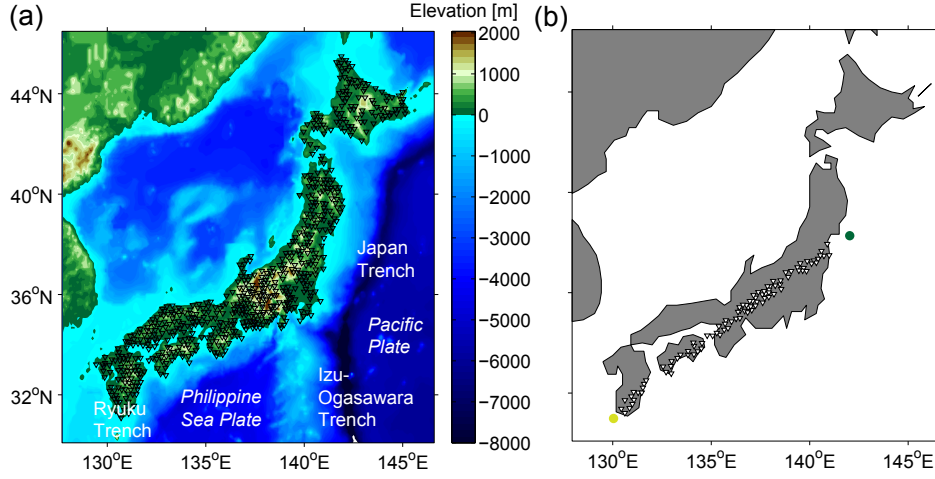


**Figure 2.** (a) a topography/bathymetry map of Japan and surroundings with the Hi-net seismic network (black triangles). (b) Configuration for measuring the Earth's rotation: one line of tiltmeter stations (triangles) illuminated from both sides by earthquakes (dots). There is a gap in the station distribution between the westernmost island (Kyushu) and the island east of Kyushu: Shikoku.

both predominantly circularly polarized, the polarization and propagation velocity of the two shear wave solutions is given by

$$\hat{\mathbf{q}}_{S+} = (\hat{\mathbf{x}} - i\hat{\mathbf{y}}) + q_z \hat{\mathbf{z}} \quad \text{with} \quad c_S = \sqrt{\frac{\mu}{\rho}} + \delta c_S,$$

$$\hat{\mathbf{q}}_{S-} = (\hat{\mathbf{x}} + i\hat{\mathbf{y}}) + q_z \hat{\mathbf{z}} \quad \text{with} \quad c_S = \sqrt{\frac{\mu}{\rho}} - \delta c_S,$$
(21)

where the velocity shift  $\delta c_S$  is given by

$$\frac{\delta c_S}{c_S^{(0)}} = \frac{\Omega}{\omega} \cos \theta,$$
(22)

with  $c_S^{(0)} = \sqrt{\mu/\rho}$ . The terms  $q_z \hat{\mathbf{z}}$  in equation (21) denote that the S-waves have a slight elliptical polarization in the longitudinal direction that is akin to the slight elliptical polarization of the the  $P$ -wave.

## 2 ESTIMATION OF RAY BENDING

To estimate the change in polarization of an  $ScS2$  wave due to lateral velocity variations we use that the shear waves are polarized perpendicular to the rays. The means that when the rays are bent, the shear wave polarizations change accordingly, and we use the ray bending as a proxy for the change in shear wave polarization. We estimate this ray bending using ray perturbation theory. In doing so we use a crude model where the  $ScS2$  ray is straight and propagates through a homogeneous velocity model that is perturbed with a weak velocity perturbation. According to equation (27) of *Snieder and Sambridge* (1992) the ray perturbation  $\mathbf{r}_1$  is in this case

given by

$$\frac{d^2 \mathbf{r}_1}{ds^2} = \nabla U,$$
(23)

where  $s$  is the arc length and  $U$  is the relative slowness perturbation. For the purpose of this study we assume that the lateral ray bending is caused by horizontal velocity gradients in the upper mantle only. Taking a straight reference ray of length  $L = 12,000$  km, we assume in the estimate a constant relative slowness gradient  $\nabla U$  for arc length  $L/2 - D < s < L/2 + D$ , where  $D = 600$  km is used for the depth of the upper mantle. This model only accounts for the ray bending associated with the propagation through the upper mantle near the free surface bounce point, but since we consider the change in polarization between  $ScS$  and  $ScS2$  waves, we only need to consider the ray bending of  $ScS2$  caused by the propagation in the upper mantle near the bounce point.

For this model the solution of equation (23) is, for a ray with fixed endpoints ( $\mathbf{r}_1(s=0) = \mathbf{r}_1(s=L) = 0$ ), for a point beyond the slowness perturbation ( $s > L/2 + D$ ) given by

$$\mathbf{r}_1(s) = -\frac{1}{L} \int_{L/2-D}^{L/2+D} (L-s)s' \nabla U ds',$$
(24)

where we used the Green's function (17.43) of *Snieder and van Wijk* (2015). The ray deflection at the receiver follows by taking the derivative with respect to  $s$ :

$$\delta\varphi = \left| \frac{d\mathbf{r}_1}{ds}(L) \right| = \frac{1}{L} \int_{L/2-D}^{L/2+D} s' |\nabla U| ds',$$
(25)

Using that the slowness gradient is assumed to be constant in the upper mantle

$$\delta\varphi = D |\nabla U|,$$
(26)

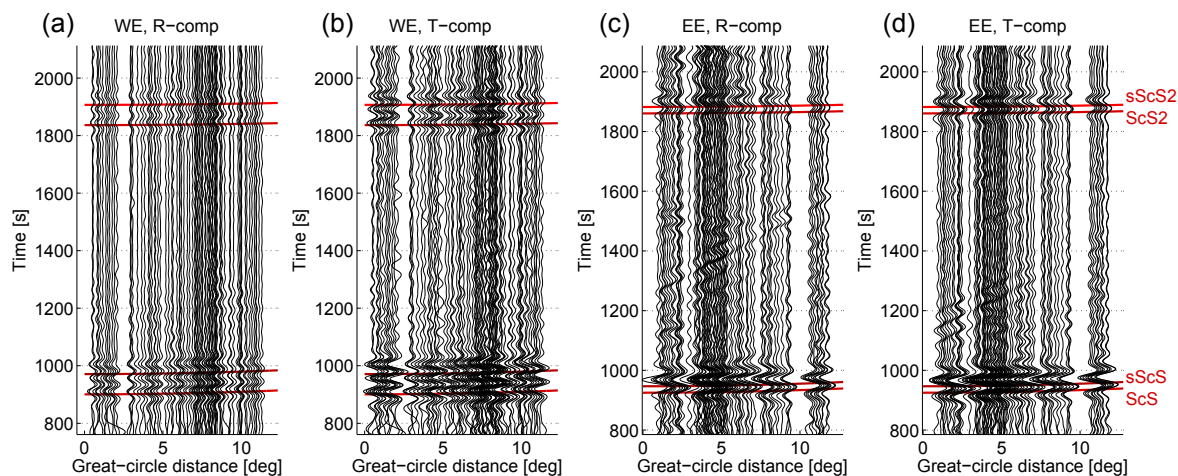


**Figure 3.** Preprocessed earthquake responses for a time window encompassing  $ScS$  and  $ScS2$ . The data is bandpass filtered between 0.01 and 0.02 Hz. (a) and (b) show the radial (R) and transverse (T) component for the westernmost event (WE, see Fig. 2(b)). (c) and (d) show the same components for the easternmost event (EE). The red lines denote the ak135 traveltimes (Kennett *et al.*, 1995) of, from early to late times,  $ScS$ ,  $sScS$ ,  $ScS2$  and  $sScS2$ .

Note that this quantity does not depend on the ray length  $L$ . For  $D = 600$  km and  $|\nabla U| = 1\%/200\text{km}$ , the ray deflection is given by  $\delta\varphi = 0.03 \approx 2^\circ$ . Note that this ray deflection is of the same order of magnitude as the change change in polarization between  $ScS2$  and  $ScS$  due to Earth’s rotation.

### 3 DATA PROCESSING OF $ScS$ AND $ScS2$ WAVES

#### 3.1 Used data

We use  $ScSn$  waves that have bounced  $n$  times between the Core Mantle Boundary (CMB) and the Earth’s surface.  $ScS2$  is a wave that reflects two times at the CMB before it was measured at the Earth’s surface. For an epicentral distance of 6 degrees, one trip back and forth to the CMB takes about 940 seconds. Hence, by detecting the polarization of  $ScS$  and of  $ScS2$ , phases with the same, but unknown initial polarization, we can detect the polarization alteration due to 940 seconds of propagation in a rotating Earth.

To make sure that the differences in polarization between  $ScS2$  and  $ScS$  are not caused by differences in source radiation, we select stations nearby an earthquake (reducing the angles of incidence to a maximum of  $3.5^\circ$ ) and in a line that also intersects the epicenter (reducing the azimuth variation at the largest used epicentral distance to  $2^\circ$ ).

Japan both has large earthquakes and a dense network of seismic stations (Obara *et al.*, 2005). We use tiltmeter recordings of the Hi-net, which is operated by the National Research Institute for Earth Science and Dis-

aster Prevention (NIED). The tiltmeters can be used as seismometers, with a high sensitivity for seismic waves with periods from tens to at least hundreds of seconds (Tonegawa *et al.*, 2006). The tiltmeters detect the tilt in two perpendicular horizontal directions. By use of the gravitational acceleration, the tilt is translated to a horizontal acceleration. After integrating once or twice, either the particle velocity or displacement is found.

Figure 2(a) shows 656 Hi-net tiltmeter stations that were active in 2005. The main tectonic units are identifiable with their imprint on bathymetry and topography. Figure 2(b) shows the locations of the used tiltmeters (green triangles) that are located near a line between two epicentres. At both ends of the line, there is a major (magnitude larger than 6) earthquake illuminating the structure below the line from opposite sides. The westernmost event (WE) is the Mw=6.2 Tanegashima (Japan) earthquake, which occurred November 21, 2005, on a depth of 150 km. The easternmost event (EE) is the Mw=7.2 Miyagi earthquake (Japan), which occurred August 16, 2005, on a depth of 40 km. The line of stations enables array processing to mitigate interference of other phases than  $ScSn$  (see next section).

#### 3.2 Processing flow

As a preprocessing, we apply rotation, bandpass filtering, time windowing, and we remove erroneous traces. The two horizontal components are rotated to the transverse and radial component, where the radial component is defined to point away from the source. In the same step, a correction is applied for the tiltmeters not being perfectly oriented to the North and East (Shiomi, 2013). We bandpass filter the earthquake responses be-

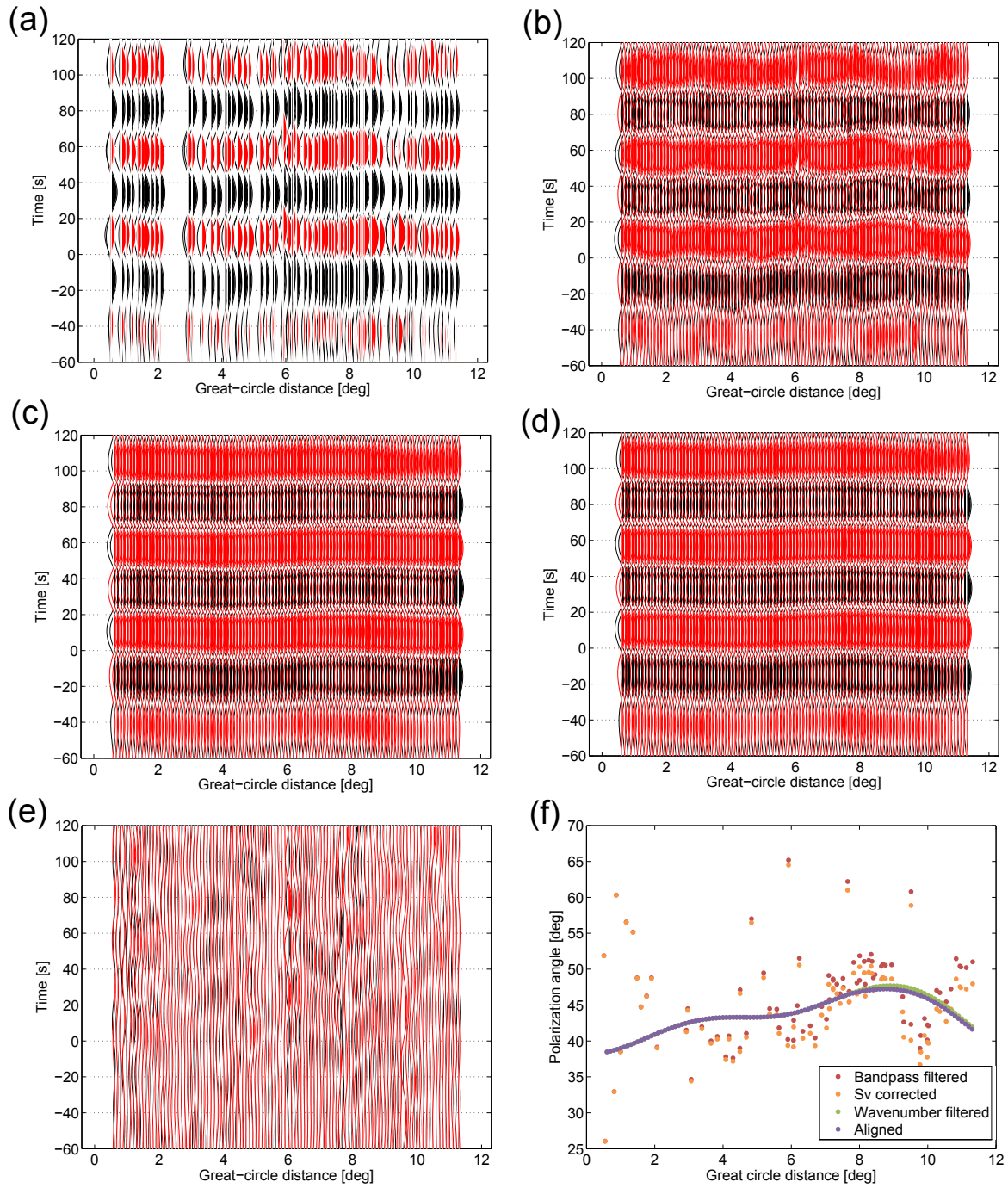


**Figure 4.** Further processing to extract the polarization, exemplified with the  $ScS$  time window of the WE: (a) bandpass-filtered, time-windowed and amplitude corrected response, (b) after spatial interpolation applied, (c) after wavenumber bandpass filtering applied and (d) after aligning the radial and transverse response. (e) the waves that have been removed by wavenumber filtering. (f) estimated polarization of  $ScS$  after the different processing steps.

tween 50 and 80 seconds. Filtering out the measurement at periods smaller than 50 seconds removes much of the complicated scattering in the upper mantle and near the CMB. We time-window the responses to a duration lasting from just before the onset of  $ScS$  to after the recording of  $ScS2$ . As a last preprocessing step we remove the few traces with poor signal to noise ratio, probably caused by instrumental issues or local noise. Fig. 3 shows the resulting responses for the WE and EE, along with expected traveltimes of  $ScS$  and  $ScS2$ , and their depth phases  $sScS$  and  $sScS2$ . The filtered data are dominated by reflections of the CMB. Yet, there are also other phases, some of which may interfere with  $ScSn$ . These additional phases may affect the estimated polarization of  $ScSn$ .

We select from the bandpass filtered data (Fig. 3) a time window around  $ScS$  and a time window around  $ScS2$ . The time windows are chosen from minus 60 to plus 120 seconds, with respect to the raytraced phase arrival time for the 1D Earth model ak135 (Kennett *et al.*, 1995). Having two events and two phases results in data in 4 time windows. We exemplify the further processing for the  $ScS$  time window of the WE. The processing for the other time windows is identical.

We apply an amplitude correction factor to the radial component. This factor corrects for the amplitude loss of the radial component that is not encountered on the transverse component. This correction does not include geometrical spreading, as this is the same for both components. The correction does include reflectivity losses for  $SV$  waves at the free surface and the CMB assuming the Earth is 1D (ak135 model). As a result, the  $SH$  waves and the amplitude-corrected  $SV$  waves are both completely reflected at the free surface and the CMB. For the largest used epicentral distance ( $12^\circ$ ) and a two-fold reflection at the CMB, the correction factor for the  $SV$  waves is about 7% of the total amplitude.

Fig. 4 shows the further steps in the data processing. Fig. 4(a) is the bandpass filtered  $ScS$  recording of the WE, time windowed between -60 and 120 seconds with respect to the ak135 arrival time. To this recording the amplitude correction has already been applied. A long wavetrain starts with  $ScS$  and then merges into  $sScS$  for later times. The radial component (black traces) has the same polarity as the transverse component (red traces). However, for plotting purposes, the polarity of the transverse component has been negated. A gap of traces, between 2 and 3 degrees, is due to a large station separation between Kyushu and Shikoku.

We spatially interpolate the data using splines to a regularly sampled distribution of epicentral distances with a spacing of  $0.1^\circ$ , yielding Fig. 4(b). From the interpolated data, phases with steep move-outs are removed through wavenumber filtering. Fig. 4(c) shows the data after wavenumber filtering, whereas Fig. 4(e) shows the data removed with wavenumber filtering. We take care

choosing the filter settings such that primarily steeply-dipping phases are removed and  $ScS$  is not affected. The same filter settings are used for both earthquakes and both phases.

Small timing mismatches occur between the radial and transverse components, either through interference with scattering from nearly flat interfaces (which are not removed by the wavenumber filter) or by anisotropy. These timing mismatches are estimated by crosscorrelating the radial with the transverse component for a time window between -10 and 50 seconds. The found delay times are subsequently used to shift one of the components, yielding Fig. 4(d). The shifts applied are much smaller than the dominant period of  $ScS$ . Hence, visually, Fig. 4(d) is almost identical to Fig. 4(c).

Finally, the polarization angle is estimated with respect to the radial component (Fig. 5), using the data variance tensor (Aster *et al.*, 1990). The polarization in the horizontal plane is measured clockwise from the radial direction and lies between 0 and 180 degrees. We use a 30 seconds time window which is centered 20 seconds after the ak135 raytraced arrival time of  $ScS$ . Fig. 4(f) shows the estimated polarizations after the different processing steps:

- (i) Red dots: After merely bandpass-filtering, the polarization shows a large scatter from station to station, primarily caused by interference by other phases and local variations in structure. Besides, a small polarization scatter is caused by azimuthal variations from station to station, as the stations are not perfectly in line.
- (ii) Orange dots: After additionally applying amplitude correction, the polarization angle is slightly reduced. The amplitude correction, and hence the polarization angle reduction, increases with distance.
- (iii) Green dots: After additionally applying wavenumber filtering, the polarization becomes much smoother as function of distance. Local perturbations, either caused by structure, by interference, or small azimuth variations, are largely removed by the wavenumber filter.
- (iv) Purple dots: After additionally applying time-alignment of both components, the polarization is only somewhat altered for the larger distances. This last processing step is more important for  $ScS2$ , for which the components show larger timing mismatches than for  $ScS$ .

Using identical processing as shown in Fig. 4, the data was prepared and the polarization was extracted for the other three time windows ( $ScS2$  of the WE and  $ScS$  and  $ScS2$  of the EE). The polarization estimated after all the processing (like the purple dots in Fig. 4(f)) are used for estimating the Earth's rotation. Fig. 5 shows the estimated polarizations as function of epicentral distance.

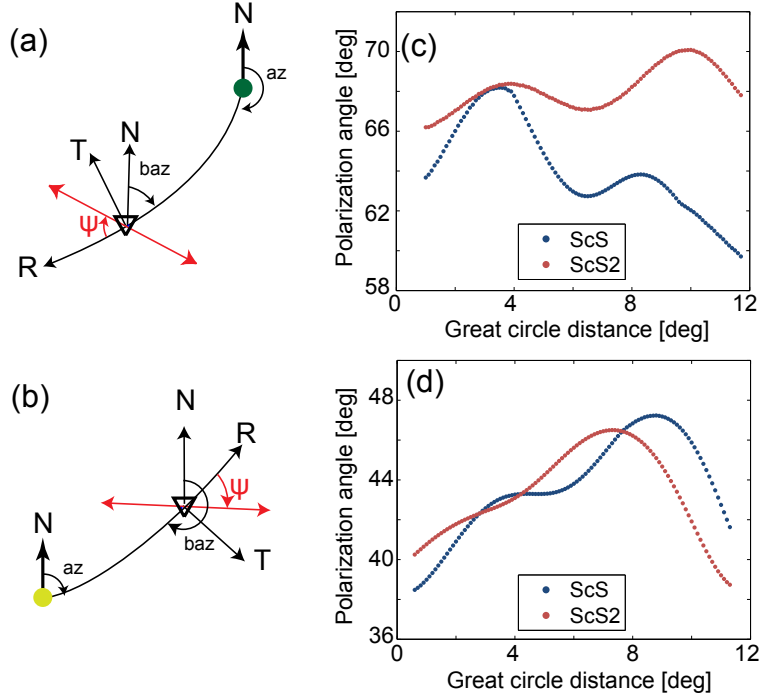


**Figure 5.** (a) and (b) are schematic source (dot) and receiver (triangle) configurations for the EE and WE, respectively. The polarization angle  $\varphi$  is defined as the clockwise angle between the radial and plane of polarization (red line). The azimuth (az) is taken at the source, as the clockwise angle between the North and the ray connecting source and receiver. The backazimuth (baz) is taken at the receiver, as the clockwise angle between the North and the ray going from the receiver to the source. The radial direction is taken opposite to the baz. (c) and (d) depict the extracted polarizations of *ScS* and *ScS2*, for the EE and WE, respectively.

### 3.3 Error propagation

In the main text, rotation-induced polarization is estimated as the difference of *ScS* and *ScS2* polarization, averaged over the WE and EE. In this section, we estimate the error of measuring the polarization of *ScS* along the receiver line  $x$  ( $\varphi_{ScS}(x)$ ) and evaluate how this error propagates into the estimation of rotation-induced polarization. The polarization of *ScS* along the receiver line is a function of:

- $\varphi_{src}$ : the source polarization, which includes both the moment tensor and the structural perturbation near the source,
- $\varphi_{struc}$ : the structural polarization perturbation (Section 2) below the receiver array, and
- $\varphi_{rot}$ : the rotation-induced polarization perturbation (see main text).

The take-off angles at the source vary little over the array, for the different *ScS* source-receiver paths. Also, the *ScS* travel times show little variation over the array. Thus, we assume  $\varphi_{src}$  and  $\varphi_{rot}$  to be constant. Hence, when removing the mean from  $\varphi_{ScS}(x)$  a perturbation remains due to receiver structure and to additive noise in waveforms:  $\varphi_{struc}(x) - \bar{\varphi}_{struc} + \varphi_{noise}(x)$ , where  $\bar{\varphi}_{struc}$

notes the mean value over  $x$  and  $\varphi_{noise}$  is a spurious term due to remaining noise. The de-meaned *ScS* polarization functions are shown in Fig. 6. For the WE, the *ScS* propagation is from west to east along the receiver line, as indicated with the yellow arrow. For the EE, the propagation direction is opposite. When following the directions of the ray as indicated by the arrows, it can be seen that where the polarization for the WE goes up, it goes down for EE, and vice versa. This observation confirms that the structural polarization perturbations are opposite for oppositely traveling waves.

We use the difference of the functions in Fig. 6 to estimate the error of measuring  $\varphi_{ScS}$ . This difference would be zero if the configuration were perfect, the equipment were ideal, the processing perfectly cancelled all the noise and introduced no errors by itself. The mean and standard deviation of the difference of the functions in Fig. 6 are  $0^\circ$  and  $0.83^\circ$ , respectively. Assuming the errors on recording  $\varphi_{ScS}(x)$  from the WE and EE are independent, the standard deviation of the error of  $\varphi_{ScS}(x)$  reads  $\sigma = 0.83^\circ/\sqrt{2} = 0.59^\circ$ .

In the main text, we compute the S-wave polarization change by taking the difference between  $\varphi_{ScS}(x)$  and  $\varphi_{ScS2}(x)$ . Assuming the errors on measuring  $\varphi_{ScS}$  and  $\varphi_{ScS2}$  to be identical and independent, the stan-

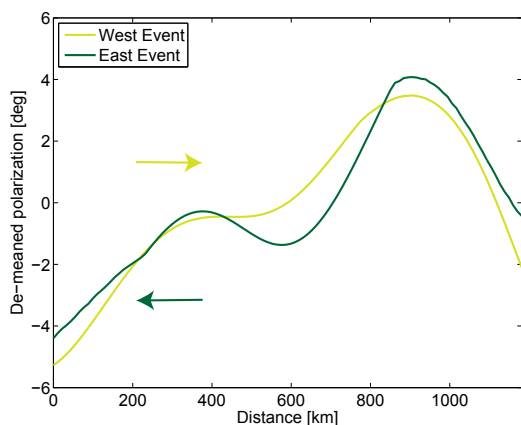


**Figure 6.** Similarity of  $ScS$  polarization along the receiver line (fig. 2b) between the West Event (yellow line) and the East Event (green line). The receiver distance is with respect to the westernmost receiver in the line. The arrows denote the direction of wave propagation along the line.

standard deviation  $\sigma$  of the error of detecting this difference equals  $0.83^\circ$ . In the main text, the rotation-induced polarization change (light-green line in figure 3c) is estimated by averaging  $\varphi_{ScS2}(x) - \varphi_{ScS}(x)$  over both events. This results in a mean value  $\mu(x)$  that is estimated with an error  $\sigma = 0.83^\circ/\sqrt{2} = 0.59^\circ$ .

## REFERENCES

- Aki, K., and P. Richards (2002), *Quantitative Seismology*, second ed., 700 pp., Univ. Science Books, Sausalito.
- Aster, R., P. Shearer, and J. Berger (1990), Quantitative measurements of shear wave polarizations at the Anza seismic network, southern California: Implications for shear wave splitting and earthquake prediction, *Journal of Geophysical Research: Solid Earth*, *95*, 12,449–12,473.
- Kennett, B., E. Engdahl, and R. Buland (1995), Constraints on seismic velocities in the earth from travel-times, *Geophys. J. Int.*, *122*, 108–124.
- Obara, K., K. Kasahara, S. Hori, and Y. Okada (2005), A densely distributed high-sensitivity seismograph network in Japan: Hi-net by National Research Institute for Earth Science and Disaster Prevention, *Rev. Sci. Instrum.*, *76*, 021,301, doi:10.1063/1.1854197.
- Shiomi, K. (2013), New measurements of sensor orientation at NIED Hi-net stations, *NIED report*, [http://dil-opac.bosai.go.jp/publication/nied\\_report/PDF/80/80-1shiomi.pdf](http://dil-opac.bosai.go.jp/publication/nied_report/PDF/80/80-1shiomi.pdf).
- Snieder, R., and M. Sambridge (1992), Ray perturbation theory for travel times and raypaths in 3-D heterogeneous media, *Geophys. J. Int.*, *109*, 294–322.
- Snieder, R., and K. van Wijk (2015), *A Guided Tour of*

*Mathematical Methods for the Physical Sciences*, 3rd ed., 560 pp., Cambridge Univ. Press, Cambridge, UK. Tonegawa, T., K. Hirahara, T. Shibutani, and K. Shiomi (2006), Upper mantle imaging beneath the Japan islands by Hi-net tiltmeter recordings, *Earth, Planets and Space*, *58*(8), 1007–1012.